The Journal of
Physical Chemistry
Letters

pubs.acs.org/JPCL Letter

# Charge Redistribution Mechanisms in $SnSe_2$ Surfaces Exposed to Oxidative and Humid Environments and Their Related Influence on Chemical Sensing

Gianluca D'Olimpio, Francesca Genuzio, Tevfik Onur Menteş, Valentina Paolucci, Chia-Nung Kuo, Amjad Al Taleb, Chin Shan Lue, Piero Torelli, Daniel Farías, Andrea Locatelli, Danil W. Boukhvalov, Carlo Cantalini,* and Antonio Politano*

**Cite This:** *J. Phys. Chem. Lett.* 2020, 11, 9003−9011

Read Online

ACCESS | Metrics & More | Article Recommendations | Supporting Information

**ABSTRACT:** Tin diselenide ($SnSe_2$) is a van der Waals semiconductor, which spontaneously forms a subnanometric $SnO_2$ skin once exposed to air. Here, by means of surface-science spectroscopies and density functional theory, we have investigated the charge redistribution at the $SnO_2$−$SnSe_2$ heterojunction in both oxidative and humid environments. Explicitly, we find that the work function of the pristine $SnSe_2$ surface increases by 0.23 and 0.40 eV upon exposure to $O_2$ and air, respectively, with a charge transfer reaching 0.56 $e^-$/$SnO_2$ between the underlying $SnSe_2$ and the $SnO_2$ skin. Remarkably, both pristine $SnSe_2$ and defective $SnSe_2$ display chemical inertness toward water, in contrast to other metal chalcogenides. Conversely, the $SnO_2$−$SnSe_2$ interface formed upon surface oxidation is highly reactive toward water, with subsequent implications for $SnSe_2$-based devices working in ambient humidity, including chemical sensors. Our findings also imply that recent reports on humidity sensing with $SnSe_2$ should be reinterpreted, considering the pivotal role of the oxide skin in the interaction with water molecules.

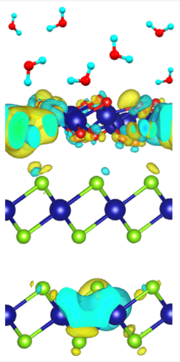

After the advent of graphene,[1−3] van der Waals semiconductors are attracting considerable attention, owing to their application capabilities that are often complementary to those of graphene,[4−6] with the subsequent prospect of novel disruptive technologies in different technological areas.[4,7,8] This class of materials is characterized by weak van der Waals bonds between layers enabling their cleavage by mechanical[9] and liquid-phase[10] exfoliation. Among van der Waals semiconductors, several materials show serious drawbacks, limiting their technological potential. Specifically, $MoS_2$ and $WS_2$ display intrinsic electron mobility as low as some tens of $cm^2$ $V^{-1}$ $s^{-1}$ at 300 K;[11] black phosphorus rapidly degrades in air due to surface oxidation;[12,13] GaSe is affected by both environmental and laser-induced degradation;[14,15] and $PdSe_2$[16] has a limited commercial potential, due to the constantly growing price of Pd (\$2000−2400/oz), which nearly doubled from 2019 to 2020.

Tin diselenide ($SnSe_2$) is a van der Waals semiconductor with a $CdI_2$-type crystal structure,[17] belonging to the $P\bar{3}m1$ space group, with tin (Sn) atoms interweaved between two hexagonally packed atomic layers of selenium (Se) (see the atomic structure in Figure S1a,b).[18,19] $SnSe_2$ shows its high intrinsic electron mobility (462.6 $cm^2$ $V^{-1}$ $s^{-1}$ at 300 K[20]) and ultralow thermal conductivity (3.82 W $m^{-1}$ $K^{-1}$[20]). It displays pressure-induced periodic lattice distortion, and moreover, it enables novel device functionalities being a phase change memory material; i.e., its atomic structure can reversibly switch from amorphous to crystalline upon laser heating, with consequent remarkable variations in optical reflectivity. Because of these peculiarities, $SnSe_2$ has high application capabilities in numerous fields, including photocatalysis,[21,22] superconductivity,[23,24] Li-ion[18,25,26] and Na-ion[18,26,27] batteries, photodetection,[28] saturable absorbers for eye-safe lasers,[29] and thermoelectricity.[30−32] Furthermore, $SnSe_2$ was used as a co-catalyst for hydrogen evolution reaction.[33]

However, all Sn-based chalcogenides are usually affected by rapid surface degradation with the emergence of tin oxide phases.[34,35] Additionally, the oxidation of starting element Sn during the synthesis can also influence the transport properties of the resulting crystal. Therefore, technological exploitation of Sn-based chalcogenides remains particularly challenging. Especially, the stability of $SnSe_2$-based devices in the ambient atmosphere is related to the chemical reactivity of its surface.

Recently, it has been shown that, though stoichiometric $SnSe_2$ shows outstanding chemical stability under ambient conditions, the presence of Se vacancies drastically affects surface chemical reactivity.[36] The $SnSe_{2-x}$ surface is trans-

**Received:** August 26, 2020
**Accepted:** October 1, 2020
**Published:** October 9, 2020

https://dx.doi.org/10.1021/acs.jpclett.0c02616

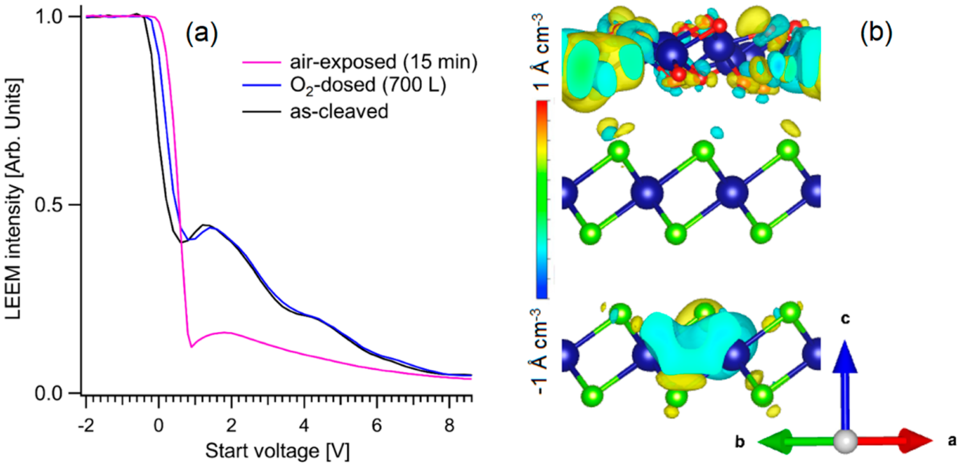

**Figure 1.** (a) LEEM $I-V$ curves at the MEM−LEEM transition for the as-cleaved sample (black), after a dose of 700 L of $O_2$ (blue), and after air exposure for 15 min (pink). The shift of the MEM−LEEM transition, characterized by the sharp decrease in intensity, indicates an oxidation-induced modification of the surface potential. (b) Changes in charge density after the formation of the interface between the $SnSe_2$ substrate and $SnO_2$ skin. Sn, Se, and O atoms are represented as dark blue, light green, and red balls, respectively.

formed into $SnO_2$ skin-terminated $SnSe_2$, with the thickness of the $SnO_2$ skin estimated to be subnanometric.[36] Unexpectedly, the self-assembled heterostructure formed by exploiting the natural interaction with air is particularly appropriate for ultrasensitive gas sensing, as demonstrated for $NO_2$ and $H_2$ with sensitivities of (1.06 ± 0.03) and (0.43 ± 0.02) ppm$^{-1}$.[36] Remarkably, such sensors are effective under dry air conditions, while previously devised $SnSe_2$ sensors used $N_2$ as the carrier gas.[37,38] Moreover, the $NO_2$ sensitivity of the $SnO_2$−$SnSe_2$ heterostructure is significantly higher compared to those of sensors based on other van der Waals semiconductors and their heterostructures.[39,40]

Remarkably, the oxide skin plays a pivotal role in $NO_2$ and $H_2$ sensing, congruently with the abundant literature on $SnO_2$-based sensors.[41−50] The modulation of resistivity upon gas adsorption is strictly connected to charge distribution in the sensing material, ultimately related to the formation of surface dipoles at the $SnO_2$−$SnSe_2$ heterojunction arising from local charge redistribution. Thus, to understand the conduction mechanism ruling chemical sensing, it is crucial to shed light on charge redistribution at the $SnO_2$−$SnSe_2$ heterostructure by measuring work-function changes. Furthermore, sensing experiments in ref 36 were carried out in dry air; thus, stability in a humid environment remains unexplored, although real conditions mandatorily require sensors to work in a changing humidity background[51,52] (not only humidity sensors[53,54]). Despite the relevance of the influence of the humid environment for practical applications, surprisingly it has been scarcely investigated, although previous reports indicated a decrease in resistance under exposure to a humid atmosphere,[51,52] which represents an unambiguous fingerprint that $H_2O$ behaves as a reducing gas in the interaction with the $SnO_2$ surface.

In addition, the interaction with water is relevant also for understanding the stability of any other $SnSe_2$-based (opto)-electronic device[55] working in ambient humidity, as well as the eventual environmental doping effects in transport properties.[56] Actually, recently different groups have reported that $SnSe_2$ is extremely sensitive to humid environments,[37,38,57] with the possibility of using it in humidity-sensing devices.

Here, we unveil the surface properties of $SnSe_2$ single crystals and their modifications in oxidative and humid environments by means of surface-science experiments and density functional theory (DFT). Definitely, surface oxidation induces an increase in the work function of 0.4 eV, owing to the charge transfer between the substrate and the $SnO_2$ skin of 0.56 e$^-$ per $SnO_2$ unit. As opposed to previous reports,[37,38,57] the pristine $SnSe_2$ surface is inert to water at room temperature, while the $SnO_2$−$SnSe_2$ heterostructure displays notable sensitivity to humidity.

The presence of the $SnO_2$ skin in the $SnSe_2$ surface exposed to oxidative environments was ensured by both microscopic evidence from low-energy electron microscopy (LEEM) (Figure S5) and vibrational experiments from high-resolution electron energy loss spectroscopy (HREELS) (Figure S6).

The analysis of the variation of work function $\Delta\Phi$ probed by LEEM could provide important insights into charge redistribution arising from surface oxidation (Figure 1a), as the total reflectivity threshold in electron backscattering (the MEM−LEEM transition, where MEM stands for mirror electron microscopy) represents a direct measurement of the variation of the surface potential.[58] Explicitly, we find $\Delta\Phi$ to be 0.23 eV for the $SnSe_2$ surface modified by exposure to 700 L of $O_2$ at room temperature, while air exposure for 15 min induces a further shift in the work function, resulting in a total increase of 0.40 eV. The observed value of $\Delta\Phi$ can be explained by considering the activation of surface dipoles, due to charge transfer at the interface from substrate to adsorbed oxygen atoms. The electronegativity of oxygen makes its adsorption generally associated with a charge transfer from the substrate to the adsorbate layer, with a subsequent increase in the work function.[59] Considering that the work function of the pristine $SnSe_2$ single crystal is ∼4.6 eV,[60] while that of $SnO_2$ is known to be ∼4.9 eV[61] (although its value can be tuned by reduction reactions[62]), both the sign and the magnitude of the experimental value of $\Delta\Phi$ are consistent with surface oxidation, involving the formation of a subnanometric $SnO_2$ skin. We can infer that previous experimental studies reporting a work function of $SnSe_2$ of (5.0 ± 0.1) eV[63,64] could be affected by surface oxidation, which generates a self-assembled $SnO_2$−$SnSe_2$ heterostructure with an increased work function. To verify this statement, we calculated $\Delta\Phi$ for the oxidation of the pristine $SnSe_2$ surface, finding a value of 0.52 eV in qualitative agreement with experimental measurements. We

**Table 1. Differential Enthalpies ($\Delta H_{ads}$), Differential Gibbs Free Energies of Physisorption ($\Delta G$), and Differential Enthalpies of Decomposition ($\Delta H_{dec}$) for Molecular Oxygen and Water on Pristine $SnSe_2$, $SnSe_{1.88}$, and SnSe Surfaces**[a]

| | | physisorption | | decomposition |
|---|---|---|---|---|
| surface | adsorbant | $\Delta H_{ads}$ (kJ/mol) | $\Delta G$ (kJ/mol) | $\Delta H_{dec}$ (kJ/mol) |
| $SnSe_2$ | $O_2$ | −17.46 | −3.16 | −42.28 (−161.58/∼−40.2) |
| | $H_2O$ | −13.27 | 18.03 | 220.91 |
| $SnSe_{1.88}$ | $O_2$ | −37.58 | −26.28 | −135.67 (−99.05/−406.65) |
| | $H_2O$ | −27.93 | 3.37 | 175.61 |
| SnSe | $O_2$ | −11.53 | −0.23 | −236.03 (−323.10/95.4) |
| | $H_2O$ | −8.12 | 23.18 | 82.22 |
| $SnO_2$ skin | $H_2O$ | −119.70 | −106.67 | −121.31 |

[a] For oxygen decomposition, the table also displays the differential enthalpy of the oxidation of the whole surface with formation of SnO and $SnO_2$-like layers (in parentheses).

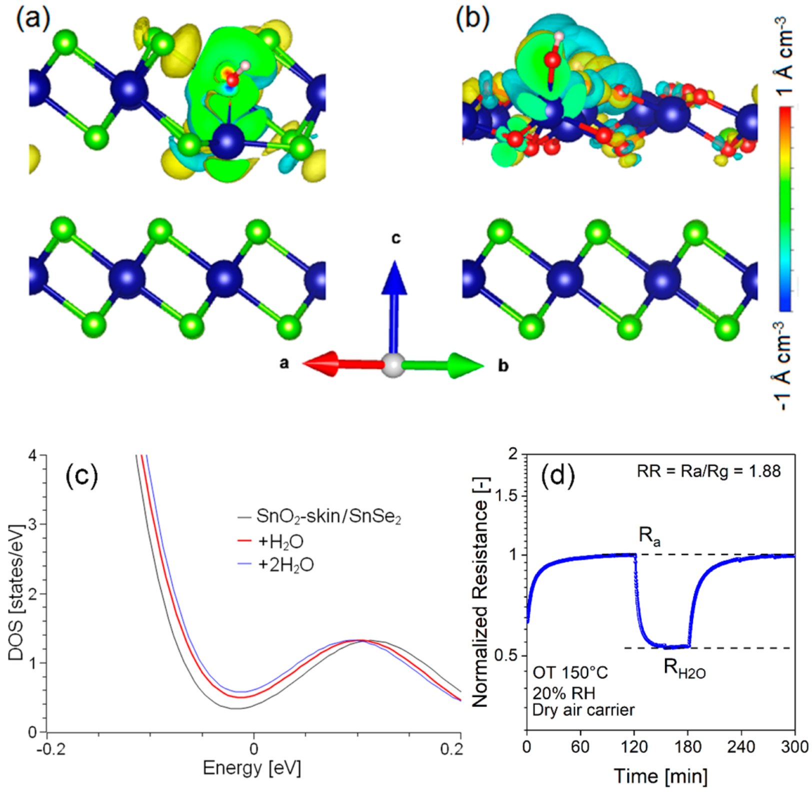

**Figure 2.** Changes in charge density after adsorption of one water molecule on (a) $SnSe_2$ and (b) $SnO_2$ skin-terminated $SnSe_2$. Panel c represents the DOS of $SnO_2$ skin-terminated $SnSe_2$ (black) and of the same system modified by the adsorption of one (red) and two (blue) water molecules. The Fermi level is set at 0. Panel d shows the response of the $SnSe_2$−$SnO_2$ heterostructure to 20% relative humidity (RH) at an operational temperature (OT) of 150 °C (note that the average residence time of the gas in the cell is approximately 10 min).

also note that, in the air-exposed sample, variations in the *I*−*V* curve associated with electron diffraction from a surface with crystalline order[65] are suppressed, due to the formation of a disordered surface oxide phase.

Complementary information about the electronic properties of the $SnO_2$−$SnSe_2$ heterostructure was achieved by comparing the surface excitation spectrum probed by electron energy loss spectroscopy (EELS) with the theoretical density of states (DOS) (section S4 of the Supporting Information). The impact of defects on the DOS is assessed in section S5.

To estimate the amount of charge transfer between the $SnSe_2$ substrate and the $SnO_2$ skin, we calculated the charge density distribution of (i) one $SnO_2$ layer over two layers of $SnSe_2$ (to model the $SnO_2$−$SnSe_2$ heterostructure), (ii) a free-standing $SnO_2$ single unit, and (ii) a bilayer of $SnSe_2$. Then, we calculated the difference between the charge densities of the whole $SnO_2$−$SnSe_2$ interface and those one of its components (single $SnO_2$ unit and bilayer $SnSe_2$). The obtained charge density difference (Figure 1b) illustrates charge redistribution following the formation of the $SnO_2$−$SnSe_2$ interface. The integration of the charge density difference along the *c* axis provides information regarding the charge transfer between the $SnSe_2$ substrate and the $SnO_2$ skin. Note that the formation of the $SnO_2$−$SnSe_2$ interface provides changes in the charge density difference in not only the outermost $SnSe_2$ layer but also the subsurface area, namely the second $SnSe_2$ layer. Definitely, the charge transfer is estimated to be 0.56 $e^-$ per $SnO_2$ unit.

While the adsorption of $O_2$ with further decomposition is energetically favorable on $SnSe_2$ (negative values of $\Delta G$ and $\Delta H_{dec}$), as well as on $SnSe_{1.88}$ and SnSe (Table 1), our theoretical model indicates that water does not adsorb on

$SnSe_2$. The energy cost for water adsorption is decreased in the presence of Se vacancies ($SnSe_{1.88}$) down to ∼3 kJ/mol, although water adsorption (as well as decomposition) remains energetically unfavorable. Similarly, SnSe also shows outstanding chemical inertness toward water.

Considering that the yield of chemical reactions also depends on the probability of the interactions between reactants, we calculated Langmuir adsorption isotherms (Figure S12). Specifically, the combination of thermodynamic and kinetic calculations evidences that the largest part of the $SnSe_x$ surface will be oxidized under experimental conditions (72% and 75% for $SnSe_2$ and $SnSe_{1.88}$, respectively).

On the contrary, the saturation coverage for water at room temperature is just 0.01 ML (with ML being monolayer) for $SnSe_2$ and $SnSe_{1.88}$, while the full coverage (1 ML) is reached upon exposing the $SnO_2$ skin to only $5 \times 10^{-3}$ L of $H_2O$ below 500 °C, thus evidencing the aptness of the $SnO_2$−$SnSe_2$ interface for ultrasensitive humidity sensing. The increase in temperature corresponds to a decrease in the sticking coefficient, with monolayer saturation reached at 0.05 and 10 L at 500 and 800 °C, respectively. Thus, the $SnO_2$−$SnSe_2$ heterostructure remains rather sensitive even at high operational temperatures.

Therefore, the $SnO_2$−$SnSe_2$ heterostructure shows superior chemical reactivity toward ambient species with respect to $SnSe_2$. On the pristine $SnSe_2$ surface, the local rearrangement of chemical bonds around each adsorbed water molecule is the origin of a redistribution of the charge density in the surface layer of $SnSe_2$ with a charge transfer of 0.17 $e^-$ per water molecule (Figure 2a). Correspondingly, water adsorption on $SnSe_2$ and $SnSe_{1.88}$ surfaces is energetically unfavorable for temperatures above 124 and 264 K, respectively (Figure S11). Hence, we conclude that pristine $SnSe_2$ is stable in a humid environment and, consequently, is unsuitable for humidity sensing, contrarily to conclusions in refs 37, 38, and 57 On the contrary, adsorption of $H_2O$ on the $SnO_2$−$SnSe_2$ heterostructure (Figure 2b) is energetically favorable even above room temperature (Figure S11). The values of charge transferred from $H_2O$ to the $SnO_2$ skin are 0.43 and 0.30 $e^-$ for one and two $H_2O$ molecules per supercell, respectively. Correspondingly, DOS (Figure 2c) is modified with a direct correlation with the coverage of the adsorbate, hence proving the appropriateness for humidity sensing also at low concentrations of $H_2O$.

Note that decomposition of a water molecule on the $SnO_2$ skin-terminated $SnSe_2$ is an exothermic process (see Table 1), although the energy gain from this process is moderate (−121.31 kJ/mol) and further water splitting is unfavorable, supporting the possible reversibility of the process.

The $SnO_2$−$SnSe_2$ heterostructure was tested as a humidity sensor (Figure 2d) at an operational temperature of 150 °C. Our devised humidity sensor exhibited (i) full recovery of the baseline resistance after water desorption and (ii) high sensitivity to water molecules, measured as the relative response (RR, the ratio between the resistance in dry air, $R_a$, and $R_{H_2O}$, the resistance in a humid environment), and an experimental limit of detection (LOD) in terms of relative humidity (RH) as low as 20% (Figure 2d).

Recently, different authors[37,38,57] have reported the outstanding performances of $SnSe_2$ in humidity-sensing devices. Our findings elucidate the key role of the surface oxide skin in the interaction with a humid environment. On the contrary, in refs 37, 38, and 57, surface oxidation was not assessed; thus, the mechanism ruling humidity sensing discussed therein should be reinterpreted.

Theoretical results were validated by surface-science techniques. In particular, HREELS experiments on water-dosed Sn-based selenides (SnSe, $SnSe_{1.4}$, $SnSe_{1.7}$, and $SnSe_2$) indicate the absence of chemisorbed water-derived species, as indicated by the lack of O−H stretching at 408−425 meV (molecular water) and 445−460 meV (hydroxyl groups) in spectra in Figure 3 (see ref 66 for more details). These findings are consistent with the positive differential Gibbs free energy of adsorption (corresponding to energetically unfavorable water adsorption) in Table 1. For the sake of comparison, we report in Figure 3 also vibrational data obtained after exposure to the same dose of $H_2O$ ($10^5$ L, with 1 L = $1 \times 10^{-6}$ Torr s) at room temperature the surface of other metal chalcogenides, which instead enable the stable adsorption of water molecules ($PtTe_{1.6}$) and hydroxyl groups (InSe).

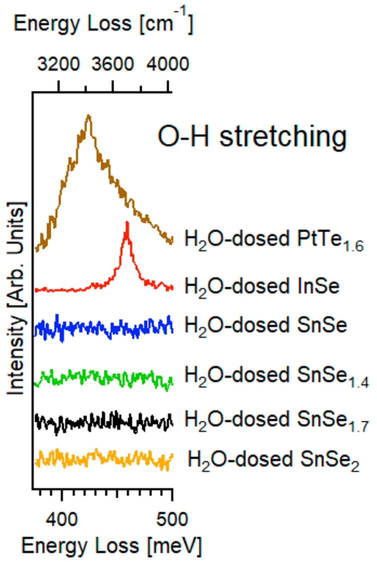

**Figure 3.** HREELS spectra in the region of the O−H band acquired after exposure to $10^5$ L of $H_2O$ at room temperature the surfaces of different Sn-based chalcogenides: $SnSe_2$ (orange curve), $SnSe_{1.7}$ (black), $SnSe_{1.4}$ (green), and SnSe (blue). To provide a straightforward comparison, the figure also displays data for $H_2O$-dosed InSe (red) and $PtTe_{1.6}$ (brown) surfaces ($10^5$ L at room temperature). The impinging energy is 4 eV.

The absence of reactivity toward water of Sn-based chalcogenides makes them suitable for catalysis (especially, photocatalytic water splitting[22] and hydrogen evolution reaction[67]) and drug delivery[68] (also considering that neither Sn nor Se is toxic). Congruently, $SnSe_2$ was used as a co-catalyst in combination with $TiO_2$ for hydrogen evolution reaction.[33]

Further information about the surface chemical bonds is gained by the inspection of core levels via X-ray photoelectron spectroscopy (XPS) experiments. Figure 4 shows the Sn-3d and Se-3d core levels of the $SnSe_2$ single-crystal surface cleaved in ultrahigh vacuum and for the same surface modified by $O_2$ and $H_2O$ dosage with a total dose of $10^5$ L. The Sn-3$d_{5/2}$ core level in the as-cleaved surface displayed a binding energy (BE) of 486.8 eV (Figure 4b). Congruently, the Se-3$d_{5/2}$ core level had a single component at a BE of 54.1 eV, in agreement with previous results for $SnSe_2$[69] and with a shift of +0.4 eV

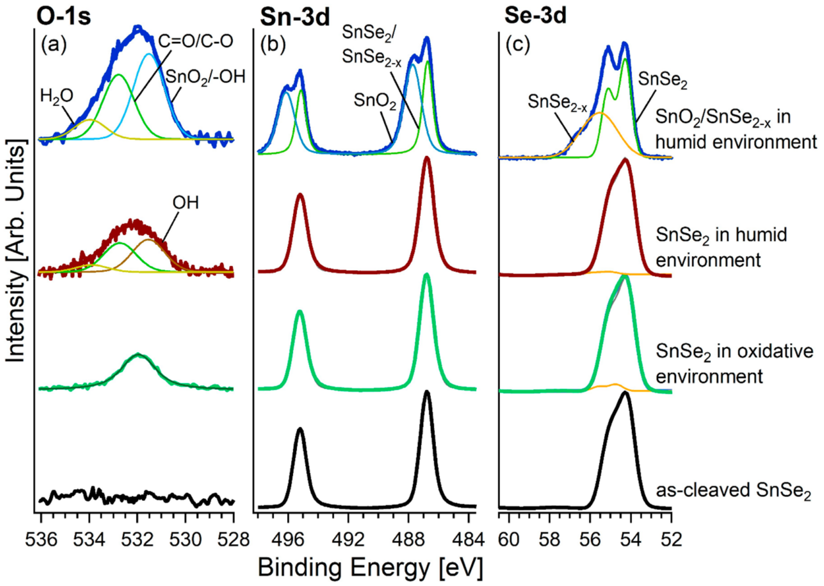

**Figure 4.** (a) O-1s, (b) Sn-3d, and (c) Se-3d core levels for the pristine surface of $SnSe_2$ cleaved in situ under ultra-high-vacuum conditions and its alteration after exposure to oxidative ($10^5$ L of $O_2$) and humid ($10^5$ L of $H_2O$) environments at room temperature. The photon energy is 800 eV. We also report in each panel the corresponding spectrum for $SnO_2$−$SnSe_{2-x}$ exposed to a humid environment at room temperature, with $x$ estimated to be 0.29.

compared to the case of SnSe. Surface treatments, i.e., $10^5$ L of $O_2$ and $H_2O$ exposure, induce only slight changes in Se-3d core levels. A novel doublet appeared in Se-3d (BE = 53.7 eV for $3d_{5/2}$), whose total spectral area is 5.4% (for $O_2$ dosage) and 2.6% (for air exposure), arising from Se(0) segregation.[70] In particular, from the analysis of Se-3d core-level spectra (Figure 4c), we can infer the absence of O−Se−O bonds, which would have a BE of ∼59−60 eV.[71−73] Congruently, the intensity of the O-1s peak is especially small in $SnSe_2$ exposed to both an oxidative and humid environment (Figure 4a); thus, we can evaluate the amount of oxygen to be <0.04 ML, due to a particularly weak sticking coefficient for oxygen adsorption at 300 K on $SnSe_2$, with the $O_2$ sticking coefficient being $<10^{-5}$.

On the contrary, we observed quite distinct peaks in $SnO_2$−$SnSe_{2-x}$ exposed to a humid environment (outermost spectra in the various panels of Figure 4), and a Sn-3d doublet with a $J$ = $^5/_2$ component is present at a BE of 487.8 eV, due to $SnO_2$ (relative amplitude of 54%), which is consistent with previous reports for this system.[74,75] Remarkably, no trace of O−Se−O bonds is present, as suggested by the lack of Se-3d components at 59−60 eV.[72] This result confirms theoretical expectations that Se is involved in only a metastable oxide phase, which represents a precursor for $SnO_2$ formation. Nevertheless, a broad spectral component in Se-3d suggests a different oxidation state for Se. In particular, the peak at 55.0 eV is ascribed to $Se^{2-}$, while that one at a higher BE should be attributed to $Se^{-2+\alpha}$ ($0 < \alpha < 1$).[76] The analysis of survey XPS spectra enables us to evaluate $\alpha$ as ∼0.145, corresponding to substoichiometric $SnSe_{1.71}$. Congruently with the results in ref 36, oxidation is feasible only in substoichiometric $SnSe_{2-x}$, while perfectly stoichiometric $SnSe_2$ is robust in oxidative environments, thus evidencing the pivotal role of Se vacancies in surface oxidation.

The O-1s spectrum for the $SnSe_2$ surface exposed to a humid environment shows new components arising from −OH groups (relative amplitude of 45%) and $H_2O$ (relative amplitude of 9%) at BEs of 531.6 and 533.6 eV, respectively.[77−79] We also exposed the $SnO_2$−$SnSe_2$ heterostructure to the humid environment, with the corresponding O-1s spectrum displaying the $SnO_2$ component (relative amplitude of 50%) at a BE of 531.5 eV,[80,81] overlapped with the −OH component.

In conclusion, we investigated (i) the modifications of surface properties once pristine $SnSe_2$ assumes a subnanometric $SnO_2$ skin upon interaction with oxidative environments and (ii) the subsequent implications for chemical sensors. Definitely, the oxidation process has a direct effect on the work function, which is increased by 0.4 eV, owing to the charge transfer between the substrate and the $SnO_2$ skin of 0.56 $e^-$ per $SnO_2$ unit. Though the $SnSe_2$ surface is inert to water at room temperature, upon surface oxidation the $SnO_2$−$SnSe_2$ interface shows a remarkable sensitivity to humidity. The charge transfer from $H_2O$ to the $SnO_2$ skin is estimated to be 0.43 and 0.30 $e^-$ for one and two $H_2O$ molecules per supercell, respectively. Correspondingly, the DOS is correlated with water coverage, hence proving the aptness for humidity sensing also at low concentrations of $H_2O$. Definitely, our findings prove the significant influence of humid environments on the electrical response of the $SnO_2$−$SnSe_2$ heterostructure. Moreover, recent reports regarding the use of $SnSe_2$ in humidity sensors should be reconsidered with regard to the physicochemical mechanism.

## ■ METHODS

Theoretical methods are described in section S8.

The single crystals were grown by the Bridgman−Stockbarger method, according to the procedure described in refs 36 and 82 (see also section S1). Their crystalline quality was secured by X-ray diffraction (XRD) (Figures S1c and S2). The analysis of the XPS survey spectrum proves the absence of contaminants in bulk crystals (Figure S3). Samples were exfoliated in situ for surface-science investigations, by using scotch tape. Gas dosage was carried out at a partial pressure of $10^{-4}$ mbar.

XPS experiments were carried out at the APE-HE beamline at the Elettra-Trieste synchrotron. Core-level measurements were performed with an Omicron EA125 hemispherical electron energy analyzer, with the sample at room temperature and in normal emission. Linearly polarized light formed an angle of 45° with respect to the perpendicular direction of the surface. After the subtraction of a Shirley background, Sn-3d core-level spectra were analyzed by using a Gaussian line shape convoluted with a Doniach−Sunjic function,[83] while Se-3d and O-1s were fitted by Voigt line shapes.

HREELS experiments were performed with an Ibach-type spectrometer. The primary electron beam energy was 3.5 eV. HREELS spectra were recorded under specular conditions.

Measurements of LEEM images (Figure S4), EELS (Figure S6), and work-function changes $\Delta\Phi$ (Figure 1a) were carried out at the soft X-ray beamline Nanospectroscopy at Elettra-Trieste synchrotron, using an energy-filtered LEEM−PEEM microscope with a spatial resolution of 10 nm. Specifically, measurements of $\Delta\Phi$ were carried out by varying the electron beam energy across the total electron reflectivity threshold. This threshold is commonly termed the MEM−LEEM transition, which is characterized by a steep decrease in intensity as a function of a bias voltage applied to the sample (start voltage) as a decelerating potential. The $\Delta\Phi$ value is identified by the shifts in the bias potential corresponding to the MEM−LEEM transition.

The gas sensing response to humidity at an operating temperature of 150 °C was determined by a volt−amperometric technique, as reported in ref 36. The RH air stream at 20% RH was obtained by mixing dry with saturated water-vapor air. In the analysis of the gas response, the relative response (RR) is defined as the ratio between the measured electrical resistance in dry air ($R_a$) and that under 20% RH ($R_{H_2O}$).

## ■ ASSOCIATED CONTENT

### Supporting Information

The Supporting Information is available free of charge at https://pubs.acs.org/doi/10.1021/acs.jpclett.0c02616.

> Single-crystal growth (section S1), LEEM images (section S2), vibrational spectroscopy (section S3), electronic properties (section S4), density of states in pristine and defective $SnSe_2$ (section S5), temperature dependence of the differential Gibbs free energy for adsorption of ambient gases (section S6), Langmuir isotherm calculations (section S7), and methods (section S8) (PDF)

## ■ AUTHOR INFORMATION

### Corresponding Authors

**Antonio Politano** − *Department of Physical and Chemical Sciences, University of L'Aquila, 67100 L'Aquila, AQ, Italy; CNR-IMM Istituto per la Microelettronica e Microsistemi, I-95121 Catania, Italy;* orcid.org/0000-0002-4254-2102; Email: antonio.politano@univaq.it

**Carlo Cantalini** − *Department of Industrial and Information Engineering and Economics, University of L'Aquila, I-67100 L'Aquila, Italy*; Email: carlo.cantalini@ing.univaq.it

### Authors

**Gianluca D'Olimpio** − *Department of Physical and Chemical Sciences, University of L'Aquila, 67100 L'Aquila, AQ, Italy*

**Francesca Genuzio** − *Elettra-Sincrotrone S.C.p.A., 34149 Trieste, Italy;* orcid.org/0000-0003-0699-2525

**Tevfik Onur Menteş** − *Elettra-Sincrotrone S.C.p.A., 34149 Trieste, Italy*

**Valentina Paolucci** − *Department of Industrial and Information Engineering and Economics, University of L'Aquila, I-67100 L'Aquila, Italy;* orcid.org/0000-0003-0641-7926

**Chia-Nung Kuo** − *Department of Physics, National Cheng Kung University, 70101 Tainan, Taiwan*

**Amjad Al Taleb** − *Departamento de Física de la Materia Condensada, Universidad Autónoma de Madrid, 28049 Madrid, Spain*

**Chin Shan Lue** − *Department of Physics, National Cheng Kung University, 70101 Tainan, Taiwan*

**Piero Torelli** − *Elettra-Sincrotrone S.C.p.A., 34149 Trieste, Italy; Consiglio Nazionale delle Ricerche (CNR)-Istituto Officina dei Materiali (IOM), 34149 Trieste, Italy*

**Daniel Farías** − *Departamento de Física de la Materia Condensada, Instituto 'Nicolás Cabrera', and Condensed Matter Physics Center (IFIMAC), Universidad Autónoma de Madrid, 28049 Madrid, Spain;* orcid.org/0000-0002-8537-8074

**Andrea Locatelli** − *Elettra-Sincrotrone S.C.p.A., 34149 Trieste, Italy;* orcid.org/0000-0002-8072-7343

**Danil W. Boukhvalov** − *College of Science, Institute of Materials Physics and Chemistry, Nanjing Forestry University, Nanjing 210037, P. R. China; Theoretical Physics and Applied Mathematics Department, Ural Federal University, 620002 Ekaterinburg, Russia;* orcid.org/0000-0002-2286-3443

Complete contact information is available at: https://pubs.acs.org/10.1021/acs.jpclett.0c02616

### Notes

The authors declare no competing financial interest.

## ■ ACKNOWLEDGMENTS

This work has been partially supported by the Spanish Ministerio de Ciencia e Innovación under Project PID2019-109525RB-I00. D.F. acknowledges financial support from the Spanish Ministry of Economy and Competitiveness, through the "María de Maeztu" Programme for Units of Excellence in R&D (CEX2018-000805-M). D.F. and A.A.T. acknowledge the project CALIPSOplus under Grant Agreement 730872 from the EU Framework Programme for Research and Innovation HORIZON 2020. A.P. and G.D. acknowledge the CERIC−ERIC Consortium for the access to the Nanospectroscopy facility and financial support. G.D. acknowledges funding of a Ph.D. fellowship from PON Ricerca e Innovazione 2014−2020 (Project E12H1800010001) by the Italian Ministry of University and Research (MIUR). D.W.B. acknowledges the support by the Ministry of Science and Higher Education of the Russian Federation (through the basic part of the government mandate, Project No. FEUZ-2020-0060).

## ■ REFERENCES

(1) Geim, A. K. Nobel Lecture: Random Walk to Graphene. *Rev. Mod. Phys.* **2011**, *83*, 851−862.

(2) Novoselov, K. S. Nobel Lecture: Graphene: Materials in the Flatland. *Rev. Mod. Phys.* **2011**, *83*, 837−849.

(3) Ambrosetti, A.; Silvestrelli, P. L. Trends in the Change in Graphene Conductivity Upon Gas Adsorption: The Relevance of Orbital Distortion. *J. Phys. Chem. Lett.* **2020**, *11*, 2737−2741.

(4) Deng, W.; Chen, X.; Li, Y.; You, C.; Chu, F.; Li, S.; An, B.; Ma, Y.; Liao, L.; Zhang, Y. Strain Effect Enhanced Ultrasensitive $MoS_2$ Nanoscroll Avalanche Photodetector. *J. Phys. Chem. Lett.* **2020**, *11*, 4490−4497.

(5) Geng, W. T.; Wang, V.; Liu, Y. C.; Ohno, T.; Nara, J. Moiré Potential, Lattice Corrugation, and Band Gap Spatial Variation in a Twist-Free $MoTe_2/MoS_2$ Heterobilayer. *J. Phys. Chem. Lett.* **2020**, *11*, 2637−2646.

(6) Zou, X.; Zhang, Z.; Chen, X.; Yakobson, B. I. Structure and Dynamics of the Electronic Heterointerfaces in $MoS_2$ by First-Principles Simulations. *J. Phys. Chem. Lett.* **2020**, *11*, 1644−1649.

(7) Guo, B. Y.; Jiang, S. D.; Tang, M. J.; Li, K.; Sun, S.; Chen, P. Y.; Zhang, S. $Mos_2$ Membranes for Organic Solvent Nanofiltration: Stability and Structural Control. *J. Phys. Chem. Lett.* **2019**, *10*, 4609−4617.

(8) Hu, C.; Jiang, Z.; Zhou, W.; Guo, M.; Yu, T.; Luo, X.; Yuan, C. Wafer-Scale Sulfur Vacancy-Rich Monolayer $MoS_2$ for Massive Hydrogen Production. *J. Phys. Chem. Lett.* **2019**, *10*, 4763−4768.

(9) Yi, M.; Shen, Z. A Review on Mechanical Exfoliation for the Scalable Production of Graphene. *J. Mater. Chem. A* **2015**, *3*, 11700−11715.

(10) Hernandez, Y.; Nicolosi, V.; Lotya, M.; Blighe, F. M.; Sun, Z.; De, S.; McGovern, I. T.; Holland, B.; Byrne, M.; Gun'ko, Y. K.; Boland, J. J.; Niraj, P.; Duesberg, G.; Krishnamurthy, S.; Goodhue, R.; Hutchison, J.; Scardaci, V.; Ferrari, A. C.; Coleman, J. N. High-Yield Production of Graphene by Liquid-Phase Exfoliation of Graphite. *Nat. Nanotechnol.* **2008**, *3*, 563−568.

(11) Jin, Z.; Li, X.; Mullen, J. T.; Kim, K. W. Intrinsic Transport Properties of Electrons and Holes in Monolayer Transition-Metal Dichalcogenides. *Phys. Rev. B: Condens. Matter Mater. Phys.* **2014**, *90*, 045422.

(12) Edmonds, M. T.; Tadich, A.; Carvalho, A.; Ziletti, A.; O'Donnell, K. M.; Koenig, S. P.; Coker, D. F.; Özyilmaz, B.; Neto, A. H. C.; Fuhrer, M. S. Creating a Stable Oxide at the Surface of Black Phosphorus. *ACS Appl. Mater. Interfaces* **2015**, *7*, 14557−14562.

(13) Kumar, A.; Telesio, F.; Forti, S.; Al-Temimy, A.; Coletti, C.; Serrano-Ruiz, M.; Caporali, M.; Peruzzini, M.; Beltram, F.; Heun, S. STM Study of Exfoliated Few Layer Black Phosphorus Annealed in Ultrahigh Vacuum. *2D Mater.* **2019**, *6*, 015005.

(14) Bergeron, A.; Ibrahim, J.; Leonelli, R.; Francoeur, S. Oxidation Dynamics of Ultrathin GaSe Probed through Raman Spectroscopy. *Appl. Phys. Lett.* **2017**, *110*, 241901.

(15) Shi, L.; Li, Q.; Ouyang, Y.; Wang, J. Effect of Illumination and Se Vacancies on Fast Oxidation of Ultrathin Gallium Selenide. *Nanoscale* **2018**, *10*, 12180−12186.

(16) Fu, M.; Liang, L.; Zou, Q.; Nguyen, G. D.; Xiao, K.; Li, A. P.; Kang, J.; Wu, Z.; Gai, Z. Defects in Highly Anisotropic Transition-Metal Dichalcogenide $PdSe_2$. *J. Phys. Chem. Lett.* **2020**, *11*, 740−746.

(17) Li, X.; Luo, N.; Chen, Y.; Zou, X.; Zhu, H. Real-Time Observing Ultrafast Carrier and Phonon Dynamics in Colloidal Tin Chalcogenide Van Der Waals Nanosheets. *J. Phys. Chem. Lett.* **2019**, *10*, 3750−3755.

(18) Wei, Z.; Wang, L.; Zhuo, M.; Ni, W.; Wang, H.; Ma, J. Layered Tin Sulfide and Selenide Anode Materials for Li- and Na-Ion Batteries. *J. Mater. Chem. A* **2018**, *6*, 12185−12214.

(19) Huang, Y.; Ling, C.; Liu, H.; Wang, S. Tuning Electronic and Magnetic Properties of $SnSe_2$ Armchair Nanoribbons Via Edge Hydrogenation. *J. Mater. Chem. C* **2014**, *2*, 10175−10183.

(20) Shafique, A.; Samad, A.; Shin, Y.-H. Ultra Low Lattice Thermal Conductivity and High Carrier Mobility of Monolayer $SnS_2$ and $SnSe_2$: A First Principles Study. *Phys. Chem. Chem. Phys.* **2017**, *19*, 20677−20683.

(21) Tan, P.; Chen, X.; Wu, L.; Shang, Y. Y.; Liu, W.; Pan, J.; Xiong, X. Hierarchical Flower-Like $Snse_2$ Supported $Ag_3PO_4$ Nanoparticles: Towards Visible Light Driven Photocatalyst with Enhanced Performance. *Appl. Catal., B* **2017**, *202*, 326−334.

(22) Fan, Y.; Wang, J.; Zhao, M. Spontaneous Full Photocatalytic Water Splitting on 2D $MoSe_2/SnSe_2$ and $WSe_2/SnSe_2$ Vdw Heterostructures. *Nanoscale* **2019**, *11*, 14836−14843.

(23) Zeng, J.; Liu, E.; Fu, Y.; Chen, Z.; Pan, C.; Wang, C.; Wang, M.; Wang, Y.; Xu, K.; Cai, S.; Yan, X.; Wang, Y.; Liu, X.; Wang, P.; Liang, S. J.; Cui, Y.; Hwang, H. Y.; Yuan, H.; Miao, F. Gate-Induced Interfacial Superconductivity in 1T-$SnSe_2$. *Nano Lett.* **2018**, *18*, 1410−1415.

(24) Shao, Z.; Fu, Z.-G.; Li, S.; Cao, Y.; Bian, Q.; Sun, H.; Zhang, Z.; Gedeon, H.; Zhang, X.; Liu, L.; Cheng, Z.; Zheng, F.; Zhang, P.; Pan, M. Strongly Compressed Few-Layered $SnSe_2$ Films Grown on a $SrTiO_3$ Substrate: The Coexistence of Charge Ordering and Enhanced Interfacial Superconductivity. *Nano Lett.* **2019**, *19*, 5304−5312.

(25) Kim, S.; Yao, Z.; Lim, J.-M.; Hersam, M. C.; Wolverton, C.; Dravid, V. P.; He, K. Lithium-Ion Batteries: Atomic-Scale Observation of Electrochemically Reversible Phase Transformations in $SnSe_2$ Single Crystals. *Adv. Mater.* **2018**, *30*, 1870393.

(26) Bai, J.; Wu, H.; Wang, S.; Zhang, G.; Feng, C.; Liu, H. Synthesis of $CoSe_2$-$SnSe_2$ Nanocube-Coated Nitrogen-Doped Carbon (NC) as Anode for Lithium and Sodium Ion Batteries. *Appl. Surf. Sci.* **2019**, *488*, 512−521.

(27) Zhang, F.; Xia, C.; Zhu, J.; Ahmed, B.; Liang, H.; Velusamy, D. B.; Schwingenschlögl, U.; Alshareef, H. N. $SnSe_2$ 2D Anodes for Advanced Sodium Ion Batteries. *Adv. Energy Mater.* **2016**, *6*, 1601188.

(28) Zhou, X.; Zhou, N.; Li, C.; Song, H.; Zhang, Q.; Hu, X.; Gan, L.; Li, H.; Lü, J.; Luo, J.; Xiong, J.; Zhai, T. Vertical Heterostructures Based on $SnSe_2/MoS_2$ for High Performance Photodetectors. *2D Mater.* **2017**, *4*, 025048.

(29) Wang, M.; Wang, Z.; Xu, X.; Duan, S.; Du, C. Tin Diselenide-Based Saturable Absorbers for Eye-Safe Pulse Lasers. *Nanotechnology* **2019**, *30*, 265703.

(30) Zhang, Y.; Liu, Y.; Lim, K. H.; Xing, C.; Li, M.; Zhang, T.; Tang, P.; Arbiol, J.; Llorca, J.; Ng, K. M.; Ibáñez, M.; Guardia, P.; Prato, M.; Cadavid, D.; Cabot, A. Tin Diselenide Molecular Precursor for Solution-Processable Thermoelectric Materials. *Angew. Chem., Int. Ed.* **2018**, *57*, 17063−17068.

(31) Luo, Y.; Zheng, Y.; Luo, Z.; Hao, S.; Du, C.; Liang, Q.; Li, Z.; Khor, K. A.; Hippalgaonkar, K.; Xu, J.; Yan, Q.; Wolverton, C.; Kanatzidis, M. G. N-Type $SnSe_2$ Oriented-Nanoplate-Based Pellets for High Thermoelectric Performance. *Adv. Energy Mater.* **2018**, *8*, 1702167.

(32) Sun, J.; Liu, S.; Wang, C.; Bai, Y.; Chen, G.; Luo, Q.; Ma, F. Interface Tuning Charge Transport and Enhanced Thermoelectric Properties in Flower-Like $SnSe_2$ Hierarchical Nanostructures. *Appl. Surf. Sci.* **2020**, *510*, 145478.

(33) Nasir, M. S.; Yang, G.; Ayub, I.; Wang, X.; Wang, S.; Nasir, A.; Yan, W. Tin Diselenide Nanoflakes Decorated Hierarchical 1D $TiO_2$ Fiber: A Robust and Highly Efficient Co-Catalyst for Hydrogen Evolution Reaction. *Appl. Surf. Sci.* **2020**, *521*, 146333.

(34) Lee, Y. K.; Luo, Z.; Cho, S. P.; Kanatzidis, M. G.; Chung, I. Surface Oxide Removal for Polycrystalline Snse Reveals near-Single-Crystal Thermoelectric Performance. *Joule* **2019**, *3*, 719−731.

(35) Lamuta, C.; Campi, D.; Pagnotta, L.; Dasadia, A.; Cupolillo, A.; Politano, A. Determination of the Mechanical Properties of SnSe, a Novel Layered Semiconductor. *J. Phys. Chem. Solids* **2018**, *116*, 306−312.

(36) Paolucci, V.; D'Olimpio, G.; Kuo, C.-N.; Lue, C. S.; Boukhvalov, D. W.; Cantalini, C.; Politano, A. Self-Assembled $SnO_2/SnSe_2$ Heterostructures: A Suitable Platform for Ultrasensitive $NO_2$ and $H_2$ Sensing. *ACS Appl. Mater. Interfaces* **2020**, *12*, 34362−34369.

(37) Pawar, M.; Kadam, S.; Late, D. J. High-Performance Sensing Behavior Using Electronic Ink of 2D $SnSe_2$ Nanosheets. *Chemistry Select* **2017**, *2*, 4068−4075.

(38) Pawbake, A. S.; Date, A.; Jadkar, S. R.; Late, D. J. Temperature Dependent Raman Spectroscopy and Sensing Behavior of Few Layer $SnSe_2$ Nanosheets. *Chemistry Select* **2016**, *1*, 5380−5387.

(39) Chen, X.; Chen, X.; Han, Y.; Su, C.; Zeng, M.; Hu, N.; Su, Y.; Zhou, Z.; Wei, H.; Yang, Z. Two-Dimensional $MoSe_2$ Nanosheets Via Liquid-Phase Exfoliation for High-Performance Room Temperature $NO_2$ Gas Sensors. *Nanotechnology* **2019**, *30*, 445503.

(40) Guo, R.; Han, Y.; Su, C.; Chen, X.; Zeng, M.; Hu, N.; Su, Y.; Zhou, Z.; Wei, H.; Yang, Z. Ultrasensitive Room Temperature $NO_2$ Sensors Based on Liquid Phase Exfoliated $WSe_2$ Nanosheets. *Sens. Actuators, B* **2019**, *300*, 127013.

(41) Zhong, Y.; Li, W.; Zhao, X.; Jiang, X.; Lin, S.; Zhen, Z.; Chen, W.; Xie, D.; Zhu, H. High-Response Room-Temperature $NO_2$ Sensor and Ultrafast Humidity Sensor Based on $SnO_2$ with Rich Oxygen Vacancy. *ACS Appl. Mater. Interfaces* **2019**, *11*, 13441−13449.

(42) Vorokhta, M.; Khalakhan, I.; Vondráček, M.; Tomeček, D.; Vorokhta, M.; Marešová, E.; Nováková, J.; Vlček, J.; Fitl, P.; Novotný, M.; Hozák, P.; Lančok, J.; Vrňata, M.; Matolínová, I.; Matolín, V. Investigation of Gas Sensing Mechanism of $SnO_2$ Based Chemiresistor Using near Ambient Pressure Xps. *Surf. Sci.* **2018**, *677*, 284−290.

(43) Das, S.; Jayaraman, V. $SnO_2$: A Comprehensive Review on Structures and Gas Sensors. *Prog. Mater. Sci.* **2014**, *66*, 112−255.

(44) Li, G.-J.; Kawi, S. High-Surface-Area $SnO_2$: A Novel Semiconductor-Oxide Gas Sensor. *Mater. Lett.* **1998**, *34*, 99−102.

(45) Di Giulio, M.; Micocci, G.; Serra, A.; Tepore, A.; Rella, R.; Siciliano, P. $SnO_2$ Thin Films for Gas Sensor Prepared by Rf Reactive Sputtering. *Sens. Actuators, B* **1995**, *25*, 465−468.

(46) Li, W.; Kan, K.; He, L.; Ma, L.; Zhang, X.; Si, J.; Ikram, M.; Ullah, M.; Khan, M.; Shi, K. Biomorphic Synthesis of 3D Mesoporous $SnO_2$ with Substantially Increased Gas-Sensing Performance at Room Temperature Using a Simple One-Pot Hydrothermal Method. *Appl. Surf. Sci.* **2020**, *512*, 145657.

(47) Li, W.; Ding, C.; Li, J.; Ren, Q.; Bai, G.; Xu, J. Sensing Mechanism of Sb, S Doped $SnO_2(110)$ Surface for CO. *Appl. Surf. Sci.* **2020**, *502*, 144140.

(48) Ko, W. C.; Kim, K. M.; Kwon, Y. J.; Choi, H.; Park, J. K.; Jeong, Y. K. ALD-Assisted Synthesis of $V_2O_5$ Nanoislands on $SnO_2$ Nanowires for Improving $NO_2$ Sensing Performance. *Appl. Surf. Sci.* **2020**, *509*, 144821.

(49) Tombak, A.; Ocak, Y. S.; Bayansal, F. $Cu/SnO_2$ Gas Sensor Fabricated by Ultrasonic Spray Pyrolysis for Effective Detection of Carbon Monoxide. *Appl. Surf. Sci.* **2019**, *493*, 1075−1082.

(50) Han, Y.; Ma, Y.; Liu, Y.; Xu, S.; Chen, X.; Zeng, M.; Hu, N.; Su, Y.; Zhou, Z.; Yang, Z. Construction of $MoS_2/SnO_2$ Heterostructures for Sensitive $NO_2$ Detection at Room Temperature. *Appl. Surf. Sci.* **2019**, *493*, 613−619.

(51) Barsan, N.; Weimar, U. Understanding the Fundamental Principles of Metal Oxide Based Gas Sensors; the Example of CO Sensing with $SnO_2$ Sensors in the Presence of Humidity. *J. Phys.: Condens. Matter* **2003**, *15*, R813.

(52) Choi, K.-I.; Hübner, M.; Haensch, A.; Kim, H.-J.; Weimar, U.; Barsan, N.; Lee, J.-H. Ambivalent Effect of Ni Loading on Gas Sensing Performance in $SnO_2$ Based Gas Sensor. *Sens. Actuators, B* **2013**, *183*, 401−410.

(53) Shelke, N. T.; Late, D. J. Hydrothermal Growth of $MoSe_2$ Nanoflowers for Photo- and Humidity Sensor Applications. *Sens. Actuators, A* **2019**, *295*, 160−168.

(54) Gupta, S. P.; Pawbake, A. S.; Sathe, B. R.; Late, D. J.; Walke, P. S. Superior Humidity Sensor and Photodetector of Mesoporous ZnO Nanosheets at Room Temperature. *Sens. Actuators, B* **2019**, *293*, 83−92.

(55) Theillet, P.-O.; Pierron, O. Quantifying Adsorbed Water Monolayers on Silicon Mems Resonators Exposed to Humid Environments. *Sens. Actuators, A* **2011**, *171*, 375−380.

(56) Panchal, V.; Giusca, C. E.; Lartsev, A.; Martin, N. A.; Cassidy, N.; Myers-Ward, R. L.; Gaskill, D. K.; Kazakova, O. Atmospheric Doping Effects in Epitaxial Graphene: Correlation of Local and Global Electrical Studies. *2D Mater.* **2016**, *3*, 015006.

(57) Tannarana, M.; Pataniya, P. M.; Bhakhar, S. A.; Solanki, G. K.; Valand, J.; Narayan, S.; Patel, K. D.; Jha, P. K.; Pathak, V. M. Humidity Sensor Based on Two-Dimensional $SnSe_2$/MWCNTs Nanohybrid for the Online Monitoring of Human Respiration and Touchless Positioning Interface. *ACS Sustainable Chem. Eng.* **2020**, *8*, 12595−12602.

(58) Nataf, G. F.; Grysan, P.; Guennou, M.; Kreisel, J.; Martinotti, D.; Rountree, C. L.; Mathieu, C.; Barrett, N. Low Energy Electron Imaging of Domains and Domain Walls in Magnesium-Doped Lithium Niobate. *Sci. Rep.* **2016**, *6*, 33098.

(59) Leung, T.; Kao, C.; Su, W.; Feng, Y.; Chan, C. Relationship between Surface Dipole, Work Function and Charge Transfer: Some Exceptions to an Established Rule. *Phys. Rev. B: Condens. Matter Mater. Phys.* **2003**, *68*, 195408.

(60) Roy, T.; Tosun, M.; Hettick, M.; Ahn, G. H.; Hu, C.; Javey, A. 2D-2D Tunneling Field-Effect Transistors Using $WSe_2/SnSe_2$ Heterostructures. *Appl. Phys. Lett.* **2016**, *108*, 083111.

(61) Li, F.; Gao, X.; Wang, R.; Zhang, T.; Lu, G. Study on $TiO_2$-$SnO_2$ Core-Shell Heterostructure Nanofibers with Different Work Function and Its Application in Gas Sensor. *Sens. Actuators, B* **2017**, *248*, 812−819.

(62) Batzill, M.; Katsiev, K.; Burst, J. M.; Losovyj, Y.; Bergermayer, W.; Tanaka, I.; Diebold, U. Tuning Surface Properties of $SnO_2(101)$ by Reduction. *J. Phys. Chem. Solids* **2006**, *67*, 1923−1929.

(63) Serna, M. I.; Hasan, S. M.; Nam, S.; El Bouanani, L.; Moreno, S.; Choi, H.; Alshareef, H. N.; Minary-Jolandan, M.; Quevedo-Lopez, M. A. Low-Temperature Deposition of Layered $SnSe_2$ for Heterojunction Diodes. *Adv. Mater. Interfaces* **2018**, *5*, 1800128.

(64) Zhang, Q.; Li, M.; Lochocki, E. B.; Vishwanath, S.; Liu, X.; Yan, R.; Lien, H.-H.; Dobrowolska, M.; Furdyna, J.; Shen, K. M.; et al. Band Offset and Electron Affinity of Mbe-Grown $SnSe_2$. *Appl. Phys. Lett.* **2018**, *112*, 042108.

(65) Bauer, E. *Surface Microscopy with Low Energy Electrons*; Springer, 2014; Vol. 23.

(66) Henderson, M. A. The Interaction of Water with Solid Surfaces: Fundamental Aspects Revisited. *Surf. Sci. Rep.* **2002**, *46*, 1−308.

(67) Inamdar, A. N.; Som, N. N.; Pratap, A.; Jha, P. K. Hydrogen Evolution and Oxygen Evolution Reactions of Pristine and Alkali Metal Doped $Snse_2$ Monolayer. *Int. J. Hydrogen Energy* **2020**, *45*, 18657−18665.

(68) Deng, J.; Mo, Y.; Liu, J.; Guo, R.; Zhang, Y.; Xue, W.; Zhang, Y. In Vitro Study of $SnS_2$, BiOCl and $SnS_2$-Incorporated BiOCl Inorganic Nanoparticles Used as Doxorubicin Carrier. *J. Nanosci. Nanotechnol.* **2016**, *16*, 5740−5745.

(69) Wu, S.; Liu, C.; Wu, Z.; Miao, L.; Gao, J.; Hu, X.; Chen, J.; Zheng, Y.; Wang, X.; Shen, C.; et al. Realizing Tremendous Electrical Transport Properties of Polycrystalline $SnSe_2$ by Cl-Doped and Anisotropy. *Ceram. Int.* **2019**, *45*, 82−89.

(70) Nagaraju, G.; Cha, S. M.; Sekhar, S. C.; Yu, J. S. Metallic Layered Polyester Fabric Enabled Nickel Selenide Nanostructures as Highly Conductive and Binderless Electrode with Superior Energy Storage Performance. *Adv. Energy Mater.* **2017**, *7*, 1601362.

(71) Dimitriev, Y.; Yordanov, St.; Lakov, L. The Structure of Oxide Glasses Containing $SeO_2$. *J. Non-Cryst. Solids* **2001**, *293−295*, 410−415.

(72) Bachvarova-Nedelcheva, A.; Iordanova, R.; Kostov, K. L.; Yordanov, S.; Ganev, V. Structure and Properties of a Non-Traditional Glass Containing $TeO_2$, $SeO_2$ and $MoO_3$. *Opt. Mater.* **2012**, *34*, 1781−1787.

(73) Fan, Y.; Zhuo, Y.; Li, L. $Seo_2$ Adsorption on Cao Surface: Dft and Experimental Study on the Adsorption of Multiple $SeO_2$ Molecules. *Appl. Surf. Sci.* **2017**, *420*, 465−471.

(74) Al-Hada, N. M.; Kamari, H. M.; Baqer, A. A.; Shaari, A. H.; Saion, E. Thermal Calcination-Based Production of $SnO_2$ Nanopowder: An Analysis of $Sno_2$ Nanoparticle Characteristics and Antibacterial Activities. *Nanomaterials* **2018**, *8*, 250.

(75) Zhang, W.; Li, M.; Xiao, X.; Huang, X.; Jiang, Y.; Fan, X.; Chen, L. In Situ Synthesis of Ultrasmall $Sno_2$ Quantum Dots on Nitrogen-Doped Reduced Graphene Oxide Composite as High Performance Anode Material for Lithium-Ion Batteries. *J. Alloys Compd.* **2017**, *727*, 1−7.

(76) Wakita, T.; Paris, E.; Kobayashi, K.; Terashima, K.; Hacisalihoğlu, M. Y.; Ueno, T.; Bondino, F.; Magnano, E.; Píš, I.; Olivi, L.; Akimitsu, J.; Muraoka, Y.; Yokoya, T.; Saini, N. L. The

Electronic Structure of $Ag_{1-X}Sn_{1+X}Se_2$ (X = 0.0, 0.1, 0.2, 0.25 and 1.0). *Phys. Chem. Chem. Phys.* **2017**, *19*, 26672−26678.

(77) Hoch, L. B.; Wood, T. E.; O'Brien, P. G.; Liao, K.; Reyes, L. M.; Mims, C. A.; Ozin, G. A. The Rational Design of a Single-Component Photocatalyst for Gas-Phase $Co_2$ Reduction Using Both Uv and Visible Light. *Adv. Sci.* **2014**, *1*, 1400013.

(78) Detweiler, Z. M.; Wulfsberg, S. M.; Frith, M. G.; Bocarsly, A. B.; Bernasek, S. L. The Oxidation and Surface Speciation of Indium and Indium Oxides Exposed to Atmospheric Oxidants. *Surf. Sci.* **2016**, *648*, 188−195.

(79) Nappini, S.; Matruglio, A.; Naumenko, D.; Dal Zilio, S.; Bondino, F.; Lazzarino, M.; Magnano, E. Graphene Nanobubbles on $TiO_2$ for *in-Operando* Electron Spectroscopy of Liquid-Phase Chemistry. *Nanoscale* **2017**, *9*, 4456−4466.

(80) Hong, X.; Li, S.; Wang, R.; Fu, J. Hierarchical $SnO_2$ Nanoclusters Wrapped Functionalized Carbonized Cotton Cloth for Symmetrical Supercapacitor. *J. Alloys Compd.* **2019**, *775*, 15−21.

(81) Xu, H.; Ju, J.; Li, W.; Zhang, J.; Wang, J.; Cao, B. Superior Triethylamine-Sensing Properties Based on $TiO_2/SnO_2$ N−N Heterojunction Nanosheets Directly Grown on Ceramic Tubes. *Sens. Actuators, B* **2016**, *228*, 634−642.

(82) Guo, C.; Guo, W.; Xu, H.; Zhang, L.; Chen, G.; D'Olimpio, G.; Kuo, C.-N.; Lue, C. S.; Wang, L.; Politano, A.; Chen, X.; Lu, W. Ultrasensitive Ambient-Stable $SnSe_2$-Based Broadband Photodetectors for Room-Temperature IR/THz Energy Conversion and Imaging. *2D Mater.* **2020**, *7*, 035026.

(83) Doniach, S.; Sunjic, M. Many-Electron Singularity in X-Ray Photoemission and X-Ray Line Spectra from Metals. *J. Phys. C: Solid State Phys.* **1970**, *3*, 285.